

RESEARCH ARTICLE

Phase, microstructure and service character of as-deposited and short-time heat-treated Ni-Mo alloys with mixed state

Hong Xu¹, Ning Li^{1,2*}, Qinghua Zhuo², Lirong Lu¹, Weizeng Chen²

1 Xingzhi College, Zhejiang Normal University, Jinhua, China, **2** College of Engineering of Zhejiang Normal University, Jinhua, China

* lintt515@126.com

Abstract

Considering the amorphous and nano-crystalline cluster structure and their activity, on the basis of the mixed structure Ni-Mo alloys, the crystallization kinetics of the alloys and the performance of the alloys after heat treatment with different mixed structure were studied. The phase structure and composition were determined by X-ray powder diffraction. The crystallization activation energy of the mixed structure was obtained by differential scanning calorimetry. The electrochemical activity of the mixed structure alloy was determined by electrochemical analysis. The experimental results show that the structural stability of the mixed-structure alloy is better, but the crystallization activation energy is much lower than that of the amorphous alloy. The crystallization process consists of a meta-stable structure transition and a new phase formation. The electrochemical properties of the alloy indicated that the alloy with the mixed structure has higher electrochemical activity, with higher hardness and better corrosion resistance, which results from the large true contact surface and the large number of active centers in this material structure.



OPEN ACCESS

Citation: Xu H, Li N, Zhuo Q, Lu L, Chen W (2021) Phase, microstructure and service character of as-deposited and short-time heat-treated Ni-Mo alloys with mixed state. PLoS ONE 16(5): e0249875. <https://doi.org/10.1371/journal.pone.0249875>

Editor: Hamid Reza Bakhsheshi-Rad, College of Engineering, University of Saskatchewan, CANADA

Received: April 21, 2020

Accepted: March 29, 2021

Published: May 21, 2021

Copyright: © 2021 Xu et al. This is an open access article distributed under the terms of the [Creative Commons Attribution License](https://creativecommons.org/licenses/by/4.0/), which permits unrestricted use, distribution, and reproduction in any medium, provided the original author and source are credited.

Data Availability Statement: All relevant data are within the paper.

Funding: The author(s) received no specific funding for this work.

Competing interests: The authors have declared that no competing interests exist.

1. Introduction

Amorphous alloys have been widely confirmed in the field of new materials due to their excellent physical and chemical properties with the characteristics of long-range disorder, short-range order and metastable structure. The alloys with high corrosion resistance, excellent electrochemical activity and lower hydrogen evolution over-potential etc., have been applied and developed in the aerospace industry, electromagnetics, new energy and chemical industries [1–4]. The long-range ordered and short-range ordered structure of nanocrystal materials is different from the conventional ordered and amorphous disordered structure. This owns the characteristics of amorphous state and quantum size, which leads to the unique and excellent properties, such as high corrosion resistance, high catalytic activity and high toughness [5–8]. Combining the characteristics of amorphous and nanocrystal materials, the amorphous and nanocrystal composite coating was obtained by one-time controllable parameters through the electrodeposition technology, composed with the characteristics of amorphous structure and

the nanocrystals. Among the reported electrodeposited alloy materials, Ni-Mo alloys are the excellent comprehensive material with outstanding physicochemical characteristics [9, 10]. The research on amorphous and nanocrystal Ni-Mo alloys indicates that the reactivity and stability of Ni-Mo alloys for electrocatalytic hydrogen evolution are closely related to the existence state of phase composition and microstructure. As hydrogen evolution cathodes, it shows an excellent electrochemical property due to the inner amorphous structure of the material [11–15]. The microstructure in the alloy determines the macroscopic properties of the electrode. The main feature of the amorphous state is metastable state, which directly determines the service life of the electrode in practical applications. The crystallization behavior of the amorphous state will determine the structural phase of the material, affecting the critical materials own structure and performances. For the alloy with amorphous and nanocrystal mixed structure, the existence of nanocrystals will inevitably affect the crystallization process of the amorphous alloy, the internal phase composition, amorphous content and specific surface area of the material [16], which will determine the physicochemical properties of the electrode.

In this paper, a certain amount of stabilizer and modifier are added to the base deposition solution of the amorphous Ni-Mo alloy coating to improve the deposition performance of the deposition solution. The co-coating composed with amorphous-nanocrystal mixed structure is obtained one time. Thermal analysis of the mixed structure coating was carried out by differential scanning calorimeter to obtain the crystallization transition temperature of the mixed structure. Different heat treatment temperatures effects on micro-hardness, corrosion resistance and electrical-chemical properties of the coating were investigated. The relationship between the amorphous content, composition, specific surface area and the electrode activity of the co-coatings were established and discussed.

2. Experimentals

2.1 Experimental materials and preparation

Without consideration of the influence of other impurity elements, the electrolyte was prepared with double distilled water and all the analytical reagents were of analytical grade (Sino-pharm Chemical Reagent Beijing Co., Ltd., Beijing, China). The main component content was given separately as $48.0 \text{ g}\cdot\text{L}^{-1}$ $\text{NiCO}_3\cdot 2\text{Ni}(\text{OH})_2\cdot 4\text{H}_2\text{O}$, $12.0 \text{ g}\cdot\text{L}^{-1}$ $\text{Na}_2\text{MoO}_4\cdot 2\text{H}_2\text{O}$, $50 \text{ g}\cdot\text{L}^{-1}$ $\text{Na}_3\text{C}_6\text{H}_5\text{O}_7\cdot \text{H}_2\text{O}$, $18 \text{ g}\cdot\text{L}^{-1}$ H_3BO_3 , $5 \text{ g}\cdot\text{L}^{-1}$ NH_4Cl , $2.4 \text{ g}\cdot\text{L}^{-1}$ Saccharin, $24.0 \text{ g}\cdot\text{L}^{-1}$ additives ($6.0 \text{ g}\cdot\text{L}^{-1}$ ascorbic acid, $4.0 \text{ g}\cdot\text{L}^{-1}$ sodium dodecyl benzene sulfonate, $10.0 \text{ g}\cdot\text{L}^{-1}$ and ethylenetetraaminetetraacetic acid). The additives were prepared ourselves. Deposition conditions: pH is 10.5 ± 0.2 , adjusted with 5% ammonium citrate solution. Current density was $5.6 \pm 0.1 \text{ A}\cdot\text{dm}^{-2}$, WYK-305 co-current voltage-stabilized source (Handan Dawei Electroplating Equipment Co. LTD., Handan, China) was used to control the working current density. Temperature is $33 \pm 2^\circ\text{C}$, bath temperature was controlled by DF-101S collector magnetic heating stirrer (Handan Dawei Electroplating Equipment Co. LTD., Handan, China). The deposition time was 30 min.

During the deposition process, pure nickel plate was used as anode ($w_{\text{Ni}} = 99.99\%$) and copper plate as the cathode. Before electrodeposition, the oxide film on the surface of the sample was removed. Epoxy resin was sealed on the back of the cathode. Then, the samples were degreased and activated with acetone and 10% dilute hydrochloric acid and 10% dilute nitric acid mixed solution and rinsed with distilled water. The surface area ratio between cathode and anode was 1:4, separated by 2.5–3.0 cm distance apart, submerged at the depth of 5–6 cm parallel to each other.

2.2 Composition test

The deposited coating materials were peeled off from the substrate and grinded to powder. The phase components and structure of the coating were measured by SMART APEX II single crystal X-ray diffractometer (Bruker SMART APEX II, BrukerSmart, Rheinstetten, Germany). Among them, Cu K α is used, the tube voltage is 35KV, and the scanning speed is 4°/min. The grain size is calculated using the Scherrer Equation [17]. The composition of the formed alloy is set to 100, and the coating is linearly fitted to the crystal. The proportion is determined according to the area of peak strength of crystalline phase, and the crystallinity of the formed alloy can be estimated. Its calculation formula is as follows:

$$\delta = k \frac{I_A}{I_A + I_B} \times 100\% \quad (1)$$

Where I_A is a crystalline phase, I_B is an amorphous phase, and K is a correction factor. Regardless of the actual influencing factors, $k = 1$ is generally considered.

Component analysis of the coating was carried out by complexometric titration. Ni²⁺ was titrated with 0.008mol/L EDTA standard solution by electroplating low carbon steel as cathode, stripping the obtained coating, dissolving in dilute nitric acid, adjusting pH to 8–9 with ammonia water, and using ammonium urea as indicator.

2.3 Thermal analysis experimental method

The synchronous thermal analyzer STA 449C DIL402C Luxx (NETZSCH, Germany) was used for thermal analysis and heat treatment. The heating rates were 5, 10, 20 and 30°C/min, respectively. Ar₂ atmosphere was used to protect the heating process, and the flow rate was 20 ml/min. After rising to the required temperature, the temperature was kept constant for 30min, and then cooled naturally in Ar₂ atmosphere. According to the relationship between peak temperature T_p and heating rate of DSC, the activation energy E of crystallization was calculated by the formula as follows.

$$d[\ln(\frac{\phi}{T_p^2})]/d(\frac{1}{T_p}) = -\frac{E}{R} \quad (2)$$

2.4 Determination of microhardness of coatings

The hardness of the coatings was tested by Shanghai 71–1 microhardness tester. The microhardness tester measures the diagonal length of the indentation remaining after the diagonal indentation of the diamond drill angle cone indenter is pressed into the measured object under 1–1000gf load by optical amplification. The formula for calculating hardness is as follows:

$$HV = 2P \sin(\alpha/2) / d^2 = 1854.4P / d^2 \quad (3)$$

In the formula, HV-Vickers hardness value (kgf/mm²), the angle between two opposite planes of A-Square quadrangular pyramid (specified as 136°); P is load (gf); d is indentation diagonal length (μ m). The simple size is 60×10×10(mm), coating thickness about 20–30 μ m.

2.5 Measurement of corrosion resistance of coatings by impregnation weight method

The so-called gravimetric method is a method to determine the corrosion rate of metal material by comparing the weight changes of the material before and after corrosion under certain conditions (pressure, temperature, medium concentration, etc.) after a certain corrosion time

of the corrosive medium. For uniform corrosion, according to the condition that the corrosion products are easily removed or firmly adhered to the surface of the sample, the weight loss or weight increase of metal corrosion per unit time and per unit area can be used to express the corrosion rate respectively.

$$K = (W_0 - W) / (s \times t) \quad (4)$$

Where K is corrosion rate $g/m^2 \cdot h$ (weight-increasing corrosion product not removed when K is negative, the error range of the experimental data is about 0.01mg), s sample area m^2 , t test time h , W_0 weight (g) before test and W is weight (g) after test. The balance used for the experimental weighing was an AE240 electronic analytical balance.

2.6 Electrochemical properties of alloy electrodes

A three-electrode system was used with a saturated calomel electrode as the reference electrode and a platinum electrode as the counter electrode. The copper plate substrate was used for the working electrode for the deposition-reduction process. The reference working electrode is a HMDE (Hanging Mercury Drop Electrode, SHY-217, Wuhan Gauss union Technology Co. LTD., Wuhan, China), as it was used in the paper [10]. The working electrode was the deposited Ni-Mo composite electrode with an area of 1 cm^2 (the electrode back was sealed with epoxy resin) to test the electrochemical properties of the obtained composites. The electrolyte concentration was $7 \text{ mol} \cdot \text{L}^{-1}$ NaOH solution at a temperature of $33 \pm 2^\circ \text{C}$. The electrode reaction parameters were measured to determine the reversibility of the electrode reaction with the scanning speed of 5 mV/s . French Bio-logic electrochemical workstation (MTZ-35, EC-lab Ltd., Berkshire, French) was utilized while using the matching Electrochemical Workstation software system (EC-Lab) to analyze the data.

3. Craystalline kinetics and microstructure of deposits

3.1 Crystallization kinetics of coatings

Fig 1 shows DSC patterns of the deposits Ni-Mo alloy at different heating rates. The matching number of Ni and Mo atoms and the difference of atomic size make the system a more compact stacking structure [18–20], inhibit a long-range diffusion, increase the viscosity sharply, and inhibit the nucleation and growth of crystalline phase.

In the experiment, the reaction rate dH/dt and reaction rate α at different temperatures were measured at 8 points in the temperature range of exothermic peak (T_0 is the starting crystallization temperature). The peak height of dH/dt at temperature T was measured, and the ratio of partial area $\int_0^T dH/dt$ of DSC curve to total area ΔH under DSC curve was measured. Then $d\alpha/dT$ is calculated from $d\alpha/dT = (1/\Delta H) \cdot (1/\Phi) \cdot (dH/dt)$. The $f(\alpha)$ and $g(\alpha)$ are kinetic functions, which are taken from references [7, 13, 14]. The activation energy E of crystallization can be calculated to be $3.84 \times 10^5 \text{ KJ/mol}$ by substituting the measured data into the equation for data processing.

3.2 Structure and phase of coatings at different heat treatment temperatures

Fig 2 is the X-ray diffraction patterns of Ni-Mo_{18.68} alloy coating heat-treated at different temperatures for 30 minutes. Fig 2(A) is the diffraction pattern of as-deposited coating. There are pre-peaks (After the introduction of Mo element, the self-diffraction peaks caused by the correlation between Ni-Ni atoms are observed.) in the small angle part ($2\theta \approx 29.32^\circ$). The existence of

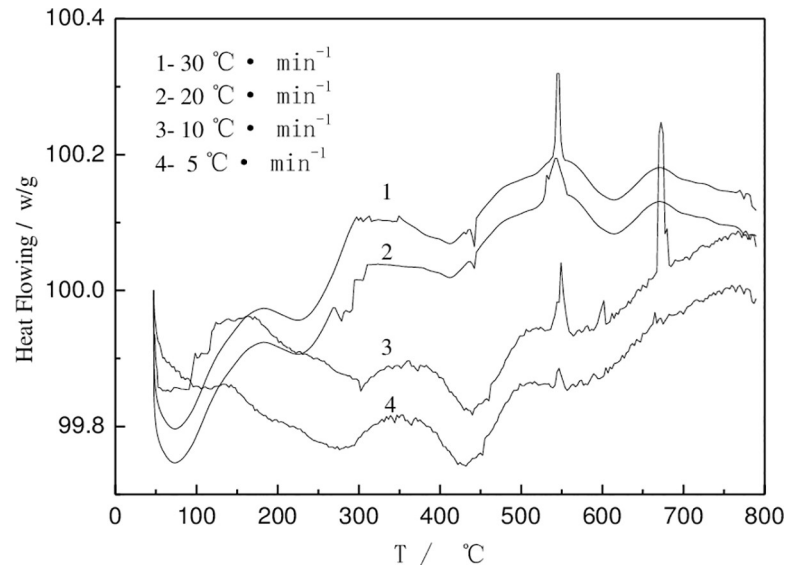


Fig 1. DSC patterns of the deposits Ni-Mo alloy at different heating rates.

<https://doi.org/10.1371/journal.pone.0249875.g001>

pre-peaks corresponds to the orientation of crystalline growth. At the same time, the stability of the corresponding short-range chemical structure is related to the stability of amorphous alloys [21–28]. Meanwhile, there is a weaker crystallization peak ($2\theta \approx 50.38^\circ$) in the diffraction peak, which indicates that there is a crystallization phase in the deposited. However, there is only one sharpened diffraction peak. This means that there is a small amount of crystalline phases distributed on the amorphous matrix. Considering of the pre-peak and the obviously broadened diffraction peaks, the obtained alloy has the ability to form a complete amorphous [24, 25].

It can also be seen from the Fig 1 that with the increase of heat treatment temperature, the coating structure gradually changes from amorphous to crystalline phase, accompanied by the formation of new phase. Fig 2(B) shows the X-ray diffraction pattern of the coating after heat treated at 250°C. After deducting the diffraction peaks of copper on the back, the amorphous diffused peaks still exist, and a strong diffraction peak appears. Linear fitting of the crystalline state of the coatings shows that the amorphous component content about 87.34%. Therefore, the coating is a mixed structure with amorphous as the main phase [26]. Compared with as-deposited structure (Fig 2A), the content of amorphous components does not decrease, but increases. The content of nanocrystals is also counted and not been calculated separately. Meanwhile the nanocrystallines in as-deposited state still have higher activation energy. During the heat treatment process, the growth direction of endothermic metals may be reversed and the azimuth angle of atomic clusters may change, with the characteristic of a widened amorphous diffraction peak at the bottom. Thermal analysis pattern shows that the structure of the coating is relaxed at about 330°C, no new phase will appear before the crystallization temperature. The strong diffraction peak may due to the increase of the ratio of metastable phase. Fig 2(C) shows the XRD pattern of heat-treated coating at 350°C. There are pre-peaks at $2\theta \approx 29.24^\circ$ and widened and symmetrical double-peak structure diffraction peaks at $2\theta \approx 43.12^\circ$, different from strong crystalline structure diffraction peaks and diffused amorphous diffraction peaks of "steamed" shape. The crystalline grains at $2\theta \approx 43.12^\circ$ calculated by Scherrer Equation were about 7.38 nm. And the crystallinity fitted by the crystalline state was about 11.48%. That's mean the coatings after heat treatment are still in the mixed amorphous and nanocrystalline structure.

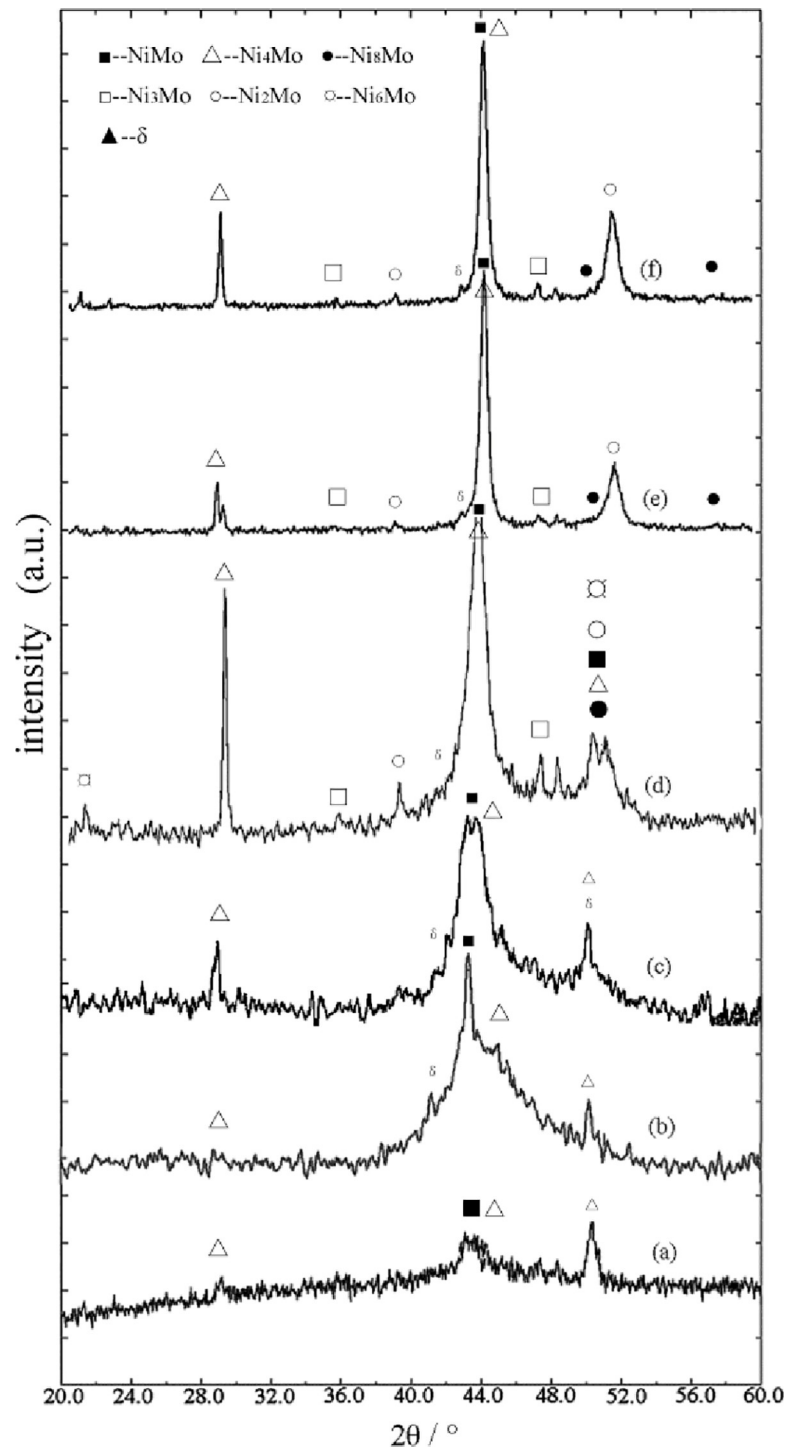


Fig 2. XRD curves of the deposited at different temperature ($t = 30\text{min}$). (a) as-deposited (b)250°C (c)350°C (d) 450°C (e)550°C (f)650°C.

<https://doi.org/10.1371/journal.pone.0249875.g002>

The diffraction intensity of the diffraction peaks of the coating heat treated at 450°C increases obviously (Fig 2D). The passive broadening at $2\theta \approx 41\sim 48^\circ$ diffraction peaks accompanies by sharp crystalline diffraction peaks. The "steamed" shape characteristics disappear

basically, and the double shoulder diffraction peaks appear at near $2\theta \approx 51^\circ$. It is inferred that the coating with mixed structure was partially crystallized at this temperature. But many amorphous phases have not translated into crystal in a short time. The structure has not been fully crystallized and still exists. Thermal analysis patterns show that the coatings begin to crystallize at 440°C , the atomic position will rearrange and new phases will appear. At the same time, the nanocrystallines begin to grow, the crystal defects in the alloy begin to increase, and the peak position becomes obvious. The amorphous phase content of the coating is estimated to be about 37.82% after linear fitting treatment, which still occupies a part of the coating. And the coating still retains the characteristics of amorphous structure. The adsorption energy of the intermetallic compounds formed with Ni and Mo atoms is different when heated, and the thermal expansion rate is different. The crystal capacity of muddy and bonding force between metal atoms are different. When the alloy is heated, the adsorption force between them is affected by the action force of the nucleus and radius of atom and the electron cloud of the high-speed rotation of the electron outside the nucleus. The metal space structure compounds with different coordination number are formed between the two atoms. The formation and growth of these compounds require higher temperature to cause the physical and chemical transformation between the alloys. The transformation of amorphous phase is delayed by the formation and growth of new phase.

Fig 2E and 2F show the diffraction patterns of the alloys at 550 and 650°C . It can be seen from the graphs that the X-ray diffraction peaks of the coatings show obvious crystallographic characteristics with the increase of heat treatment temperature. Phase analysis of as-deposited and heat-treated coatings was carried out in Table 1, in which the metastable phase is expressed by δ .

It can be seen from Table 1 that the alloy phase with mixed crystal structure obtained under deposition condition contains NiMo and Ni_4Mo phases [19]. Heat treated at 250 and 350°C in a short time, the structure of the coating remains basically unchanged, and the metastable phase remains in the alloy structure. According to the first principle calculation in document [29, 30], it is indicated that the metastable phase maybe $\text{Ni}_{24}[\text{Ni}_{4x}\text{Mo}_{4(5-x)}]\text{Mo}_{12}$ ($0 \leq x \leq 5$) with a certain stability. New phases were formed in the treated alloy after heat at 450°C , and metastable phases in the alloy structure began to change. At higher temperatures, the outermost electrons of metal atoms intensified, and the number of shared electrons changed, resulting in the formation of Ni-Mo intermetallic compounds with different spatial structures and atomic ratios. When the temperature reaches 550°C , the metastable phase in the alloy has disappeared

Table 1. The phase composition of the deposits after heat treatment.

Composition T ($^\circ\text{C}$)	NiMo	Ni_3Mo	Ni_4Mo	Ni_8Mo	Ni_2Mo	Ni_6Mo	δ	structure
as-deposited	✓		✓				✓	amp-nano
250	✓		✓				✓	amp-nano
350	✓		✓				✓	amp-nano
450	✓	✓	✓	✓	✓	✓	✓	amp-nano
550	✓	✓	✓	✓	✓			cry
650	✓	✓	✓	✓	✓			cry
$2\theta / ^\circ$	39.6	36.2 46.2	29.2					
	42.2		44.2					
	46.2		46.1					
Ref.	[20]	[20]	[20]	[27]	[28]	[21]	[29]	

Note: ✓ means existence, amp-amorphous, nano-nanocrystal, cry-crystal.

<https://doi.org/10.1371/journal.pone.0249875.t001>

and transformed into stable phase Ni_3Mo and Ni_2Mo with Ni-Mo structure. Ni_3Mo has a body-centered tetragonal structure, similar to the spatial structure of Ni_3Nb , and a good storage activity structure. Ni_2Mo has Pt_2Mo structure and shows a certain structural stability at low temperature.

Generally, the atoms in metal alloys follow a regular and orderly arrangement while growing. From Fig 2, a peak present in the diffused peak as "steamed bun" diffraction peaks of X-ray intensity curves of as-deposited amorphous alloys. The peak indicates the chemical short-range ordered structure in amorphous structure. During heat treatment, the disappearance of the pre-peak and peak indicates the short-range ordered growth in the alloy. The enhancement of the crystalline diffraction peak indicates that the growth process of atoms in the alloy is obvious. The internal structural atoms of metals are arranged in accordance with the spatial lattice of its own components, which improves the thermal stability of the alloy structure. The peak characteristics of amorphous alloys remained in the coatings treated at 450°C for 30 minutes (Fig 2(D)). This may be caused by the relatively small mobility of atoms at this temperature and in a short time, and the mobility of atoms is controlled to a certain extent. Therefore, in a short time, the alloys heat treated near the crystallization transition temperature still retain the arrangement characteristics of as-deposited metal atoms. With the further increase of temperature, the temperature difference of amorphous transition crystalline state is compensated by high temperature, so the velocity of atom movement increases in a short time, the efficiency of position rearrangement increases, and the possibility of new compounds formation increases. It can be seen from Table 1 that the intermetallic compounds Ni_2Mo and Ni_6Mo at higher temperatures enrich the spatial structure of Ni-Mo alloys.

3.3 Surface morphology of alloy coating after heat treatment

Fig 3 shows the surface topographies of the coating after heat treatment at different temperatures. The surface of the coating is basically cellular structure. With the increase of heat treatment temperature, the boundaries of cellular particles become blurred first and then clear, and the cellular particles become smaller first and then larger gradually. When the particles grow up, the intercellular space increases and the surface of the coating becomes rough. After annealing at 450°C , the morphology of the coating is basically the same as that of the as-deposited, smooth, bright, clean and flat. The boundaries are still clear, but the brightness becomes dark. It is found that the cells are packed tightly with clear boundaries, and individual shadows appear in Fig 3(B). At this time, the diffusion and migration of atoms in the plating layer may be further accelerated due to the increase of temperature. Unstable atoms are spontaneously adjusted and rearranged under higher energy, and no longer maintain the brightness in appearance. At low magnification, the blackness of cellular particles in the surface layer increases, some boundaries become blurred. Enlarged observation shows that the cellular particles are uniformly distributed and present disintegrated small "honeycombs", which is due to the higher energy further enlarging its range of motion and the migration and diffusion movement exceeded the boundary. Therefore, after heat treatment at 450°C , the morphology of the coating is dispersed on the cotton-like as of the crystallization. With the further increase of the treated temperature, XRD diffraction patterns of the coating shows that the crystallization is in a large amount with more obvious intergranular boundary and the intergranular bonding is weakened.

4. Effect of heat treatment on the performance of mixed coatings

4.1 Effect of heat treatment on microhardness of coating

Table 2 shows the average grain size and Vickers hardness of the deposited and heat-treated coatings. The data show that the grain size range is fewer changes and the hardness is relatively

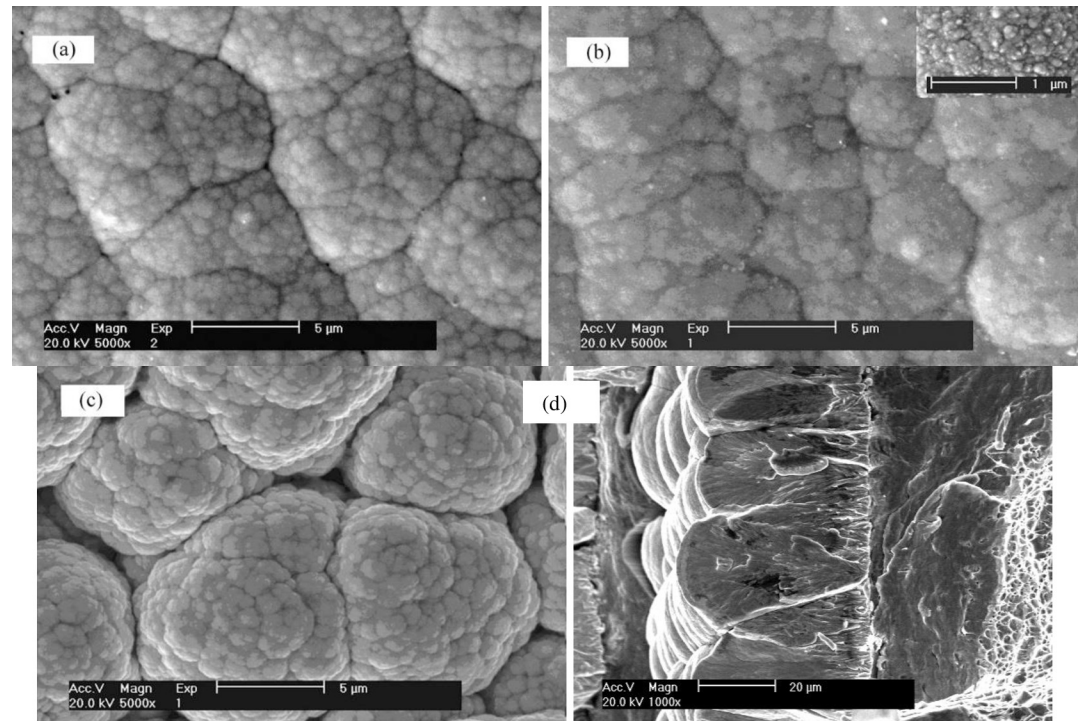


Fig 3. SEM images of the as-deposited and the deposits after heat treatment. (a) as deposited (b) 450 °C (c) 650 °C (d) cross-sectional of as-deposited.

<https://doi.org/10.1371/journal.pone.0249875.g003>

high below 350 °C. As is known to all, the characteristic of crystal grain growth of amorphous structure coating needs higher energy after structural relaxation stage. And nanocrystals themselves are unstable structures and tend to grow up when the outside world gives them higher energy. Below 350 °C, the amorphous "structural relaxation" transition occurs in the coating, and the internal short-range ordered atoms will undergo structural relaxation, and the long-range atoms will diffuse. The structure will move from a metastable state to another metastable state. When the annealing temperature increases above 400 °C, the grain growth trend gradually increases. After annealing at 650 °C for 2 hours, the average grain size of the coating increased from 3.6 nm to 45 nm. The active H atoms adsorbed inside the coating combines due to endotherm and escapes from the inside of the plating layer, so that the metal atoms inside the plating layer are compactly combined, reducing the compressive stress and the relaxation force, thereby causing the microhardness change of the plating layer. But the microstructure of the coating did not change significantly. The microhardness of the coating changes greatly with the growth of crystal grains.

The factors that generally affect the hardness of the coating are the grain structure and particle size, dislocation density and dislocations caused by impurities. The smaller the grain size of the coating, the higher the hardness, and the highest hardness of the coating at 450 °C. Combined with DSC patterns and XRD patterns of the co-coatings, the formation of a high

Table 2. The average grain size and Vickers hardness of the deposited and heat-treated samples.

Temperature (°C)	25	250	350	450	550	650
Average grain size (nm±0.1)	3.6±6	3.8±14	6.3±4.8	12.4±19	25.4±66	45±59
Vickers hardness (HV±1%)	856±23	740±21	846±13	883±13	725±17	542±19

<https://doi.org/10.1371/journal.pone.0249875.t002>

hardness Ni_3Mo phase with the quality of a brittle, high hardness, increases the microhardness of the deposition. The coatings studied in this paper have the highest hardness at 450°C , and may also be related to the formation of metastable $\text{Ni}_{24}\text{Mo}_{12}$ phase at 350°C [22, 23]. At the same time, a new phase is formed in the coating, and the growth of the crystal grains causes a large change in the microhardness of the coating. After the crystal phase transformation of the plating, the lattice distortion is caused, the plastic deformation resistance of the plating is increased, and the hardness value is higher than that of the deposited. The recombination and position rearrangement of the internal atoms of the coating make Ni and Mo combine with the new phase Ni_2Mo and Ni_6Mo , and the two phases belong to the plastic phase with a certain extension. The performance, at this time, the microhardness of the coating is significantly reduced because the formation of the crystal structure forms a large number of grain boundaries and internal defects, and the growth of the nanocrystallines causes a large angle grain boundary between them, under the action of external force. The structural defects inside the coating move rapidly. The plastic phase also slows down the external force of the crystal, and the microhardness decreases.

4.2 Effect of heat treatment on corrosion resistance of coating

Fig 4 shows the relationship between the corrosion resistance of the coating alloy in $33\pm 2^\circ\text{C}$, 0.4 mol/L NaCl solution. It can be seen from the figure that the average loss of the coating gradually increases with time until the coating is completely dissolved. The coated has less corrosion amount at room temperature, after 30 days soaked, the pattern tends to be stable, the amount of corrosion varies basically no longer changed. The corrosion loss of the coating after heat treatment at 250°C is much larger than that of the deposited. It is considered that the structural relaxation phenomenon of the coating under higher temperatures condition makes the grain boundary of the crystalline obvious. With the progress of structural relaxation, a certain new phase will be formed. These new phases reduce the corrosion resistance of the material. The corrosion resistance of the coating treated at 350°C is significantly deteriorated, and the structure

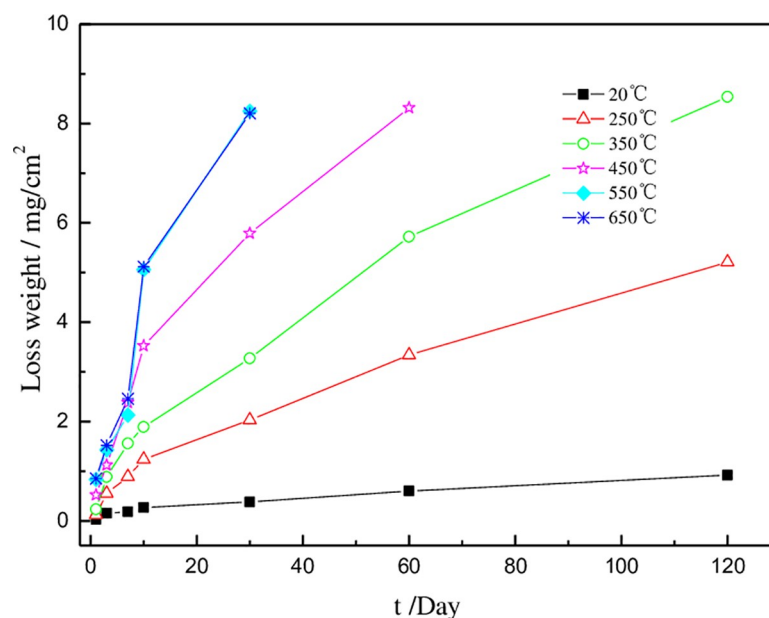


Fig 4. Average weight loss of the coatings in 0.4mol/L NaCl .

<https://doi.org/10.1371/journal.pone.0249875.g004>

of the coating becomes slack under this temperature. Some metastable phases and new nanocrystalline formed inside. The grain boundary defects reduce the corrosion performance of the material, and increase the corrosion loss amount. But the amorphous structure in the coating still has good corrosion resistance [30, 31]. When the heat treatment temperature exceeds the crystallization temperature (over 450°C), the internal defects of the nanocrystals were transferred and increased, the number of grain boundaries increased, and these structural features reduced the corrosion resistance of the coating. At the same time, the new phase produced by the recombination of Ni and Mo atoms improves the compactness of the coating, but the corrosion resistance of the coating is lowered due to the generation of many grain boundaries.

4.3 Effect of heat treatment on electrochemical properties of coatings

Taken the depositors as an electrode, a steady-state polarization pattern was performed at $33 \pm 2^\circ\text{C}$, 7 mol/L NaOH solution, as shown in Fig 5. The patterns show that with the heat treatment temperature increases, the chemical catalytic activity of the coatings increase first and then decrease. It is considered that the amorphous content is relatively high before the crystallization starts, and the content of short-range ordered atomic clusters in the alloy increases [32–35]. The slack particles also become active centers, and the activity of the deposition is increased. The treated alloy at 350°C has the best hydrogen evolution catalytic activity. It is believed that under this temperature condition, the structural relaxation of the amorphous structure completed, and the amorphous phase changes from one metastable state to another metastable structure. And the new metastable structure has higher activity energy. Thereby the treated alloy exhibited in higher catalytic activity and lower hydrogen evolution overpotential. The initial potential of the alloy electrode treated after 550°C is significantly reduced, and its catalytic activity is relatively weakened compared with the alloy containing the amorphous structure. It is considered that the existence of the amorphous structure increases the degree of disorder of the internal atomic arrangement. During the deposition progress, the H atom with larger activity and smaller radius is easily adsorbed in the disordered atomic cluster in the structure. Within the electrolysis process, it is easier to combine with itself to form an active center, and improve the catalytic activity

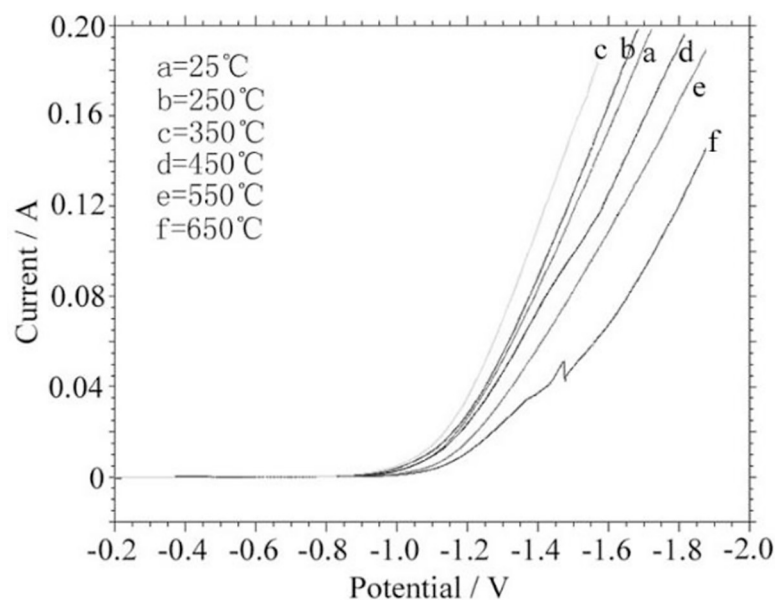


Fig 5. Steady electrode polarization patterns of the deposited after heat treatment.

<https://doi.org/10.1371/journal.pone.0249875.g005>

of the alloy electrode. The increase of catalytic activity may also be a substitutional solid solution or intermetallic compound with more activity of [Mo] and [Ni] in the alloy coating with higher Mo content, and adsorbed H with smaller radius. The atom is solid-solubilized inside the alloy structure, and increases the electrocatalytic activity of the coating. The alloy electrode (Fig 5D) treated at 450°C in a short time has a higher catalytic activity and a lower hydrogen evolution overpotential at lower current density. It is considered that the amorphous crystallization process is unstable. The new phase crystal nucleus maintains the catalytic activity of the amorphous structure and exhibits a low hydrogen evolution overpotential. At a higher current density, the alloy quickly lost its own activity. The alloy electrode treated at 650°C (Fig 5F) has a sudden change in electrode performance at -1.45 V. This phenomenon suggests that the defects inside the crystalline structure still have higher energy and rapid migration ability during the electrolysis process, at lower current density, the defects in the crystal play a certain active center. When the current density is too large, the migration speed is lower than the hydrogen evolution rate, the voltage rises rapidly, and the energy consumption increases.

4.4 EIS properties analysis of alloy electrodes

Fig 6 shows Electrochemical Impedance Spectroscopy (EIS) patterns of deposits as alloys electrodes at $33 \pm 2^\circ\text{C}$, 7 mol/L NaOH solution. Fig 6(A) shows that the EIS spectrum of the crystalline alloy after heat treatment is a single semicircle. The hydrogen evolution process is a Volmer-Heyrovsky reaction to control the hydrogen evolution process, that is, the [H] atom in the adsorbed state is electrochemically desorbed to form hydrogen. The pattern of the mixed structure alloy is composed of a half circle and an approximate straight line, and the hydrogen evolution process could be a Volmer-Tafel mechanism, that is, the [H] atom in the adsorbed state is chemically desorbed to form H_2 gas, and the rate determining step is a volmer reaction. The semicircle corresponds to the electrochemical reaction step of the electrode surface, and the semicircle diameter is approximately equal to the electrochemical reaction resistance R_r . The smaller the radius, the higher the electrochemical activity of the electrode specific surface. The analog equivalent circuit diagram for the Ni-Mo alloy is shown in Fig 6(B), and the

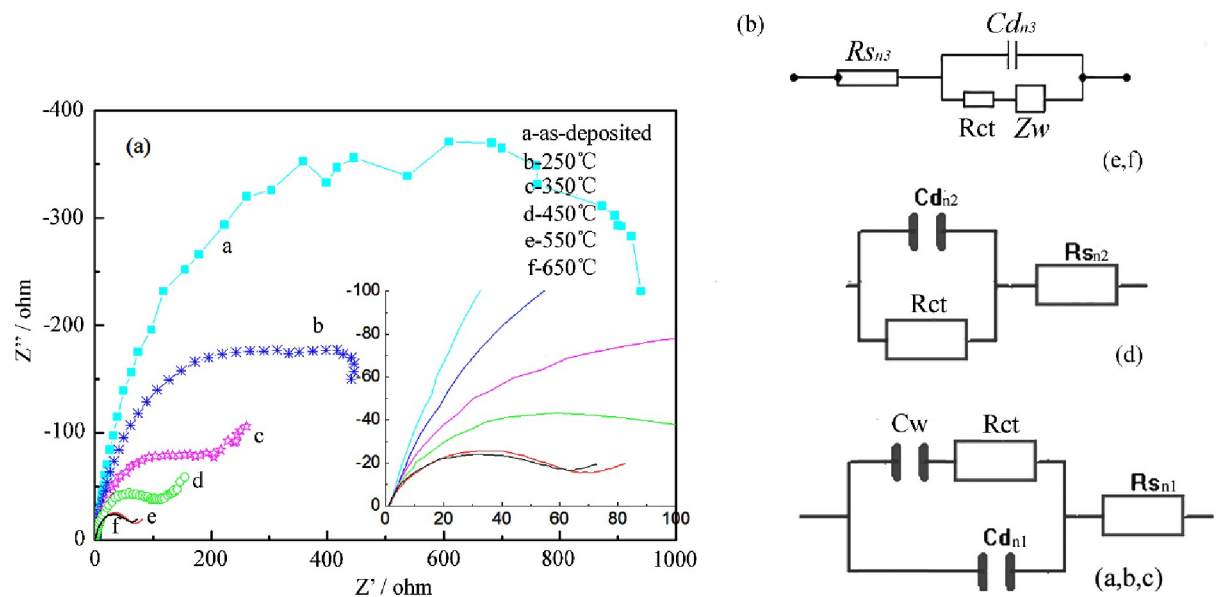


Fig 6. Electrochemical impedance spectroscopy for as-deposited and heat-treated samples (a) and equivalent circuit (b).

<https://doi.org/10.1371/journal.pone.0249875.g006>

Table 3. Equivalent circuit parameters of the various components for as-deposited and heat-treated samples.

parameters electrodes	$R_s / \Omega \text{cm}^2$	$R_{ct} / \Omega \text{cm}^2$	$C_d (\text{F}/\text{cm}^2)$	CPE	$S_{\text{real}} / \text{cm}^2$	amorphous content
650°C	5.12	60.60	3.306×10^{-3}	-	165.3	-
550°C	5.54	67.42	3.564×10^{-3}	-	178.2	-
450°C	6.43	167.87	3.786×10^{-3}	-	189.3	37.82%
350°C	5.84	315.72	2.548×10^{-3}	3.21×10^{-3}	127.4	88.52%
As-deposited	7.46	1628.12	1.286×10^{-3}	8.54×10^{-3}	64.3	86.88%
250°C	9.46	667.87	1.134×10^{-3}	7.23×10^{-3}	56.7	87.34%

<https://doi.org/10.1371/journal.pone.0249875.t003>

equivalent parameters are shown in Table 3. $R_s(n)$ represents the overall ohmic resistance of the electrolyte. R_{ct} and $C_d(n)$ are the charge transfer resistance and its related double-layer capacitance between the electrolyte and electrode. Z_w is the Warburg impedance related to the diffusion of deposition in the electrode. R_{ct} and Z_w together constitute Faraday impedance, which reflects the dynamic reaction of the battery. And a high R_{ct} generally corresponds to a relatively slow kinetics of the Faraday reaction. CPE is the smooth line or working electrode WE. C_w is the capacitance of the concentration polarization of the electrolyte. The difference between the Y-axis and X-axis value in the Nyquist curves may be related to material composition and coating structure. That is to say, the greater the difference between the component phases, the worse the stability of the coating structure and the matrix electrolyte, and the easier it is to cause the increase of polarization degree of the electrodes, which leads to the increase of mismatch degree between the electrodes. The materials microstructure XRD patterns after heat treatment show that when the temperature was higher than 450°C, the amorphous components in the film are almost absent. Fig 6(E) and 6(F) are in this state. No capacitive characteristics are shown in Electrochemical Impedance Spectroscopy of these two materials. Therefore, the fitting patterns are different with the incipient styles. And its CPE value cannot be obtained. From the fitting parameters in Table 3, the specific surface of the mixed-structure alloy increases with the increase of the amorphous content in the component, and the interaction contact between the electrode and the solution interface is increased after the heat treatment process. The resistance produces large impedance, while the generation of a new phase material with a finer grain size in the crystalline alloy increases the catalytic activity of the coating. Thereby, the increased contact surface accelerated the adsorbed [H] atom diffused, expedited hydrogen absorption and desorption, and increased the hydrogen evolution electrochemical activity of the electrode. The further growth of the crystal grains increases the crystal defects inside the deposits and increases the reactive center of the electrode after crystallization, and the new phase material changes the internal structure of the co-coating. As the degree of crystallization increases, the grain size becomes larger, the grain boundary length longer, the number of reactive centers decreases, and the catalytic activity decreases.

5. Conclusions

1. The nanocrystals in mixed structure coatings enlarges the relaxation temperature range of amorphous structure, prolongs the relaxation time, reduces the activation energy of crystallization of amorphous structure.
2. Mixed structural alloys have higher microhardness and better corrosion resistance than crystalline structural alloys, due to amorphous atomic clusters and a small amount of crystallographic defects in the alloy structure.

3. Under the condition of constant potential electrolysis, the mixed structure alloy has higher electrode catalytic activity and lower hydrogen evolution overpotential than the crystalline structure alloy, i.e. lower energy consumption, which is mainly caused by the active center of amorphous clusters and small size nanocrystals in the mixed structure.
4. The experimental data of AC impedance of alloy electrodes show that the mixed structure alloys have larger contact surface, lower self-resistance and higher electrocatalytic activity than crystalline alloys.

Acknowledgments

Thanks are due to the testing center of Zhejiang Normal University Institute of Physical Chemistry for assistance with the experiments for valuable discussion.

Author Contributions

Formal analysis: Hong Xu, Ning Li, Qinghua Zhuo, Lirong Lu, Weizeng Chen.

References

1. Li Ning, Chen Weizeng, Lu Lirong, Gao Chenghui. Electrodeposition Behavior of Polycrystalline Ni–Mo–La Composite in Alkaline Solution [J], *Coatings*, 2018, 8(9), 299–311
2. Wang Hongzhi; Lei Xianchao; Yao Suwei; Zhang Weiguo, Effect of heat treatment on properties of Ni–Sn–P coatings[J], *Surface Engineering*, 2018, 34(6): 468–474
3. Sabzi Masoud; Mousavi Anijdan Seyyed Hashem; Zadeh Mostafa Roghani; Farzam Mansour. The effect of heat treatment on corrosion behaviour of Ni-P-3 gr/lit Cu nano-composite coating[J], *Canadian Metallurgical Quarterly*, 2018, 57(3): 350–357
4. Mukhopadhyay Arkadeb; Barman Tapan Kumar; Sahoo Prasanta. Effect of Heat Treatment on the Characteristics of Electroless Ni-B, Ni-B-W and Ni-B-Mo Coatings[J], *Materials Today: Proceedings*, 2018, 5 (2): Part1, 3306–3315
5. Diego Luna, Marta Miranda, Humberto Hamad Minervino Antonio, Verónica Piñeiro, Carlos Herrero-Latorre, Marta López-Alonso, Validation of a simple sample preparation method for multielement analysis of bovine serum, *PLoS ONE*, 2019, 14(2): 1–10
6. Mousavi R.; Bahrololoom M.E.; Deflorian F., The effect of surfactant on the microstructure and corrosion resistance of electrodeposited Ni-Mo alloy coatings, *Anti-Corrosion Methods and Materials*, 2019, 66(5): 631–637
7. Vamsi M.V.N.; Wasekar Nitin P.; Sundararajan G. Influence of heat treatment on microstructure and mechanical properties of pulse electrodeposited Ni-W alloy coatings[J], *Surface and Coatings Technology*, 2017, 319: 403–414
8. Nozaki Ai, Tanihara Yasutomo, Kuwahara Yasutaka, Ohmichi Tetsutaro, Kamegawa Takashi, Mori Kohsuke, et al. Active skeletal Ni catalysts prepared from Ni–Zr amorphous alloys by oxygen treatment [J], *Applied Catalysis A: General*, 2015, 504: 559–564
9. Wojewoda-Budka J., Wierzbicka-Miernik A., Litynska-Dobrzynska L., Szczerba M.J., Mordarski G., Mosiałek M., et al., Microstructure characteristics and phase transformations of the Ni-P and Ni-P-Re electroless deposited coatings after heat treatment[J], *Electrochimica Acta*, 2016, 209: 183–191
10. Li N., Gao C.H., Yang S.Z. Crystallization Kinetics of Electrodeposited Amorphous/Nanocrystalline Ni_{81.32}Mo_{18.68} Alloy Coating[J], *Acta Physico-Chimica Sinica*, 2009, 25(4): 735–740
11. Chen Liang-Yu; Xu Tianxiang; Lu Sheng; Wang Ze-Xin; Chen Shujin; Zhang Lai-Chang. Improved hardness and wear resistance of plasma sprayed nanostructured NiCrBSi coating via short-time heat treatment[J], *Surface and Coatings Technology*, 2018, 350: 436–444
12. Guo Wei; Wang Haiyan; Jia Qiang; Peng Peng; Zhu Ying. Transient Liquid Phase Bonding of Nickel-Base Single Crystal Alloy with a Novel Ni-Cr-Co-Mo-W-Ta-Re-B Amorphous Interlayer[J], *High Temperature Materials and Processes*, 2017, 36(7): 677–682
13. Semenenko K. I.; Kashirin M. A.; Stognei O. V.; Al-Maliki A. D. Thermal stability, structure and phase composition of Ni_x(NbO)_{100-x}composites[J], *Journal of Surface Investigation. X-ray, Synchrotron and Neutron Techniques*, 2016, 10(5): 1087–1091

14. Wasekar N.P.; Verulkar S.; Vamsi M.V.N.; Sundararajan G., Influence of molybdenum on the mechanical properties, electrochemical corrosion and wear behavior of electrodeposited Ni-Mo alloy, *Surface and Coatings Technology*, 2019, 370: 298–310
15. Luo Hong, Leitch Michael, Behnamian Yashar, Ma Yongsheng, Zeng Hongbo, Luo Jing-Li. Development of electroless Ni-P/nano-WC composite coatings and investigation on its properties[J], *Surface & Coatings Technology*, 2015, 277: 99–106
16. Jin Shi-wei; Kang Min; Shao Yue; Du Xiao-xia; Zhang Xin-ying. Crystallization Process of Heat-treated Amorphous Ni-P Alloy Coating[J], *Journal of Materials Engineering*, 2016, 44(9): 115–120
17. Scherrer P. Bestimmung der Größe und der inneren Struktur von Kolloidteilchen mittels Röntgenstrahlen. In *Ein Lehrbuch Kolloidchemie* [C]; Zsigmondy R., Ed.; Springer-Verlag: Berlin, Germany, 1918; 98–100.
18. Spiller E., X-ray optics. In *Encyclopedia of Optical Engineering* [C]; Driggers R.G., Hoffman C., Driggers R., Eds.; CRC Press: Boca Raton, FL, USA, 2003; 3042–3048.
19. Jaksic J.M., Vojnovic M.V., Krstajic N.V. Kinetic Analysis of Hydrogen Evolution at Ni-Mo Alloy Electrodes[J], *Electrochimica Acta*.2000, 45(19):4151–4158.
20. Berry L.G. (Ed.) Powder Diffraction File Joint Committee on Powder Diffraction Standards, 1973.Ni: File 4–850, Ni4Mo: File 3–1036, Ni3Mo: File 17–572
21. Damian Alexis; Omanovic Sasha. Ni and NiMo hydrogen evolution electrocatalysts electrodeposited in a polyaniline matrix[J], *J. Power Sources*, 2006, 158(1): 464–476.
22. Nagai Masatoshi. Transition-metal nitrides for hydrotreating catalyst-Synthesis, surface properties, and reactivities[J], *Applied Catalysis A: General*, 2007, 322: 178–190.
23. Evard E.A., Kurdumov A.A., Berseneva F.N., Gabis I.E. Permeation of hydrogen through amorphous ferrum membrane[J], *Hydrogen Energy*, 2001, 26 (5): 457–460.
24. Binder Kurt, Kob Walter. Glassy materials and disordered solids: An introduction to their statistical mechanics [C]. World Scientific Publishing Company, 2005, 10
25. Yazdani Arash, Höhne Günther W H, Misture Scott T, Graeve Olivia A. A Method to Quantify Crystallinity in Amorphous Metal Alloys: A Differential Scanning Calorimetry Study, *PloS one*, 2020, 15(6): e0234774, <https://doi.org/10.1371/journal.pone.0234774> PMID: 32569283
26. Carr Nan Z., McLellan Rex B. The thermodynamic and kinetic behavior of metal–vacancy–hydrogen systems[J], *Acta Materialia*, 2004, 52 (11):3273–3293.
27. Zhou S.H., Wang Y., Jiang C., First-principles calculations and thermodynamic modeling of the Ni-Mo system[J], *Materials Science and Engineering A*, 2005, 397:288–296
28. Das S.K., Thomas G., Order-Disorder Transformations in Alloys[J], *Phys. Status Solidi (a)*, 1974, 21: 177–190.
29. Wang Y., Woodward C., Zhou S.H., Structure stability of Ni-Mo compounds from first-principles calculations[J], *Scripta Materialia*, 2005, 52:17–20
30. Emran Khadijah M., Al-Harbi Albandaree K., Outstanding resistance and passivation behaviour of new Fe-Co metal-metal glassy alloys in alkaline media. *PLoS ONE*, 2018, 13(1): 1–10 <https://doi.org/10.1371/journal.pone.0187567> PMID: 29337992
31. Li Y.J., Wang Y.G., An B., Xu H., Liu Y., Zhang L.C., et al. A Practical Anodic and Cathodic Curve Intersection Model to Understand Multiple Corrosion Potentials of Fe-Based Glassy Alloys in OH- Contained Solutions. *PLoS ONE*, 2016, 11(1): 1–20
32. Hertsyk ., Kovbuz ., Pereverzeva T. H., Borysyuk . K., Boichyshyn L. M. Influence of Heat Treatment and Variable Magnetic Fields on the Chemical Resistance of Amorphous Alloys Based on Iron[J], *Materials Science*, 2014, 50(3): 454–460
33. Laszczyńska A., Szczygieł I. Electrocatalytic activity for the hydrogen evolution of the electrodeposited Co-Ni-Mo, Co-Ni and Co-Mo alloy coatings. *International Journal of Hydrogen Energy*, 2020, 45(1): 508–520
34. Zhou Q.; Li Z.; Wang F. Effect of Mo on the Skeleton Structure and Hydrogen Evolution Performance of Ni-Mo Alloys Electrode Prepared by De-alloying, *Chemical Journal of Chinese Universities*, 2019, 40 (8): 1717–1725
35. Ning Li, Hong Xu, Xinhui Li, Weizeng Chen, Lijuan Zheng, Lirong Lu. Tribological properties and corrosion resistance of porous structure Ni-Mo/ZrO₂ Alloys, *Coatings*, 2020, 10(8), 767; <https://doi.org/10.3390/coatings10080767>